Geophysical Research Letters

RESEARCH LETTER
10.1029/2022GL100016

Turbulent Dissipation in the Surface Mixed Layer of an Anticyclonic Mesoscale Eddy in the South China Sea

Jihai Dong[1,2], Baylor Fox-Kemper[3], Zhiyou Jing[4,5], Qingxuan Yang[6,7], Jiwei Tian[6,7,8], and Changming Dong[1,2]

[1]School of Marine Sciences, Nanjing University of Information Science and Technology, Nanjing, China, [2]Southern Marine Science and Engineering Guangdong Laboratory (Zhuhai), Zhuhai, China, [3]Department of Earth, Environmental, and Planetary Sciences, Brown University, Providence, RI, USA, [4]State Key Laboratory of Tropical Oceanography, South China Sea Institute of Oceanology, Chinese Academy of Sciences, Guangzhou, China, [5]Southern Marine Science and Engineering Guangdong Laboratory (Guangzhou), Guangzhou, China, [6]Physical Oceanography Laboratory/IAOS and Frontiers Science Center for Deep Ocean Multispheres and Earth System, Ocean University of China, Qingdao, China, [7]Pilot National Laboratory for Marine Science and Technology, Qingdao, China, [8]Sanya Oceanographic Institution, Ocean University of China, Sanya, China

Key Points:

- Turbulent dissipation in the surface mixed layer (SML) from different dynamic processes is quantitatively clarified at an anticyclonic eddy
- Negative potential vorticity values are observed along the eddy sections and are associated with symmetric, gravitational, and centrifugal instabilities
- Symmetric instability contributes to the integrated dissipation rate in the SML by a mean magnitude of 4.3×10^{-6} W m kg^{-1}

Supporting Information:

Supporting Information may be found in the online version of this article.

Correspondence to:

J. Tian and C. Dong,
tianjw@ouc.edu.cn;
cmdong@nuit.edu.cn

Citation:

Dong, J., Fox-Kemper, B., Jing, Z., Yang, Q., Tian, J., & Dong, C. (2022). Turbulent dissipation in the surface mixed layer of an anticyclonic mesoscale eddy in the South China Sea. *Geophysical Research Letters*, *49*, e2022GL100016. https://doi.org/10.1029/2022GL100016

Received 17 JUN 2022
Accepted 4 AUG 2022

Abstract

Clarifying contributions to the surface mixed layer (SML) dissipation from dynamic processes including winds, waves, buoyancy forcing and submesoscales is of significance for quantifying exchanges between the atmosphere and the ocean. Based on two observation sections across an anticyclonic eddy in the South China Sea, the contributions from different dynamic processes to the SML dissipation rate of turbulence are quantified. The potential vorticity indicates instability events including symmetric instability (SI), gravitational instability and centrifugal instability at the eddy. Despite of a dominant role of wind- and wave-induced dissipation rates, SI is highlighted by a mean estimated depth-integrated dissipation rate of 4.3×10^{-6} W m kg^{-1} with a maximum up to 3.2×10^{-5} W m kg^{-1}. The SI dissipation is believed to play a role in the eddy kinetic energy budget by extracting energy from the vertical geostrophic shear at the eddy.

Plain Language Summary

Active dynamic processes generated by air-sea interactions drive a highly turbulent and dissipative ocean surface mixed layer (SML). It is important to clarify the contributions from these dynamic processes to the SML dissipation. Mesoscale eddies are rotating vortices with spatial scales of $O(100)$ km, which are ubiquitous over the global ocean. Strong currents and fronts at mesoscale eddies exert profound effects on the SML dynamics. Based on in situ observation sections across an anticyclonic mesoscale eddy in the South China Sea, dissipation rates from winds and waves, symmetric instability (SI) and gravitational instability are characterized at the eddy using observations combined with recent theories. Consistent with the traditional assumptions, the SML dissipation is dominated by the energy produced from winds and waves. Nonetheless, the eddy-induced vertical current shear favors a kind of smaller-scale instability in the SML, that is, SI, which feeds on the current circulating within the eddy. The dissipation due to the SI process at the eddy can reach 4.3×10^{-6} W m kg^{-1} within the SML, which is a non-negligible contribution to the energy budget.

1. Introduction

As the layer linking the atmosphere and ocean interior, the ocean surface mixed layer (SML) is the vital channel for exchanges of energy and materials. The SML is a highly turbulent layer with complex dynamic processes that modulate these exchanges, including surface forcing (e.g., winds and buoyancy fluxes) and processes in the SML (e.g., surface waves, Langmuir circulation, and submesoscale instabilities) (Large et al., 1994; McWilliams, 2016; Melville, 1996; Thorpe, 2004). Despite of the energy contained in these small-scale processes, they are rarely resolved in ocean models due to their small spatial scales (meters to kilometers) and are approximated mostly through bulk parameterizations of their effects on larger scales. Quantifying their contributions and developing parameterizations is a key topic of oceanographic research (e.g., Fox-Kemper et al., 2008, 2011; Li et al., 2016; Noh et al., 2016; Qiao et al., 2016).

Mesoscale eddies are vortices rotating about a vertical axis with spatial scales of $O(100)$ km, which dominate the kinetic energy of the ocean. The ubiquitous mesoscale eddies are important in the transport and storage of energy and materials (Dong et al., 2014; Zhang et al., 2014), and through these effects exert significant consequences in

the SML. Anticyclonic eddies deepen the SML, while cyclonic ones thin it, with anomalies up to tens of meters (Gaube et al., 2019). Surface wave characteristics are also potentially modulated at mesoscale eddies (Marechal & de Marez, 2021; Wang et al., 2020). Moreover, the strong buoyancy gradient and velocity shear within the SML associated with mesoscale eddies favor submesoscale instabilities. Legg et al. (1998) simulated the emergence of submesoscale baroclinic and symmetric instabilities at the edge of an eddy under surface cooling. Idealized mesoscale eddy simulations by Brannigan et al. (2017) also demonstrated that submesoscale instabilities feed on both vertical shear production and vertical buoyancy fluxes. All these phenomena potentially contribute to the kinetic energy budget within the SML. Haney et al. (2015) and Buckingham et al. (2019) showed how the relative contribution of different forms of kinetic energy production and dissipation can be used even in complex overlapping classes of instabilities and turbulence to categorize and compare the relative importance of different boundary layer and submesoscale processes.

However, only a few studies have been focused on examining SML dissipation in and near mesoscale eddies, and even fewer based on in situ observations (e.g., Yang et al., 2017). Turbulent kinetic energy dissipation is highly localized, following an approximately lognormal distribution (Pearson & Fox-Kemper, 2018); sampling such a variable field requires an in-depth understanding of the turbulent dissipation. Mesoscale eddies are widespread in the South China Sea (SCS) which is one of the largest marginal seas in the world (Chen et al., 2011; Lin et al., 2015; Zhang et al., 2016). Turbulent mixing contributes to mesoscale eddy dissipation (Zhang et al., 2016) and in turn high kinetic energy carried by abundant mesoscale eddies has been reported to make a great contribution to local turbulent mixing in the SCS (Yang et al., 2019). Using the same observations as the work here, Yang et al. (2017) reported that the SML dissipation is enhanced at the eddy periphery. The enhanced dissipation is qualitatively attributed to submesoscales energized by the eddy. In this work, the observed dissipation will be directly compared to the dissipation calculated from the parameterization of different SML processes to quantify their contributions and investigate the potential role of the eddy in modulating SML turbulence.

The paper is organized as follows: Section 2 introduces methods and data; Section 3 presents the quantitative analysis of the turbulent dissipation in the SML across the eddy; discussion and conclusions are in Section 4.

2. Methods and Data

2.1. Methods

2.1.1. Dissipation From Winds and Waves

The dissipation from winds and waves including Langmuir turbulence is divided into three layers (Buckingham et al., 2019; Terray et al., 1996). Within one significant wave height near the very surface, the dissipation is roughly constant and derives mainly from the energy injection by surface waves. This layer is not considered here, because all samples of the turbulence observations in this work are below 10 m, far deeper than the surface wave significant height (Figure S1 in Supporting Information S1). Below the surface breaking wave layer is a layer that is dominated by non-breaking waves. The dissipation in this layer is scaled as from Langmuir turbulence. Below this layer, turbulent dissipation is negligibly small for this analysis. Hence, the turbulent dissipation forced by winds and waves is calculated as (Buckingham et al., 2019; Terray et al., 1996),

$$\varepsilon_w = \begin{cases} \dfrac{w_{*b}{}^3}{H_s} f_b, & z_L \le z < 0 \\ \dfrac{w_{*L}{}^3}{H} f_L, & -H \le z < z_L \\ 0, & z < -H \end{cases} . \tag{1}$$

Here, $w_{*b} = \left(u_*{}^2 \bar{c}\right)^{1/3}$ is the velocity scale for the wave-breaking turbulence ($u_* = \sqrt{|\boldsymbol{\tau}_w|/\rho_0}$ is the friction velocity, τ_w is the wind stress, $\rho_0 = 1{,}024$ kg m^{-2} is the seawater density constant; $\bar{c} = 0.1 c_p$ is the effective wave speed, $c_p = gT/2\pi$ is the peak wave phase speed, T is the peak wave period), $w_{*L}{=}(u_*{}^2 u_{st})^{1/3}$ is taken as the velocity scale for the Langmuir turbulence (Grant & Belcher, 2009); u_{st} is the surface Stokes drift velocity, $f_b = 0.3(H_s/z)^2$ and $f_L = 0.23H/|z|(1{-}0.6z/H)$ describe the vertical structures of the dissipation rate within the wave-breaking and Langmuir layers, respectively (Buckingham et al., 2019); H_s and H are the significant wave height and the mixed layer depth, $z_L = 5/6H[1{-}(1 + 36/115H_s/Hc_p/u_{st})^{1/2}]$ is the transition depth between the wave-breaking and Langmuir layers. The velocity scales, w_{*b} and w_{*L} are calculated on the basis of the ERA5 wind and wave data. The

mixed layer depth H is determined as the depth where a temperature difference of 0.2°C from 10-m depth reaches (de Boyer Montégut et al., 2004). Different methods have been proposed to scale the turbulence driven by winds and waves in the SML. Given that the observed dissipation is dominated by winds and waves (see Section 3), the method used here is relatively closer to the observations compared to other methods without the Langmuir effect (Hara & Belcher, 2004; Yu et al., 2019).

2.1.2. Dissipation From Gravitational Instability

The dissipation due to gravitational instability (GI) is related to the surface buoyancy flux

$$B_0 = g\alpha \frac{Q_{\text{net\_heat}}}{\rho_0 C_P} + g\beta(EP)S, \tag{2}$$

where α is the thermal expansion coefficient, $Q_{\text{net\_heat}}$ is the net surface heat flux, $C_p = 3850$ J kg^{-1}°C^{-1} is the seawater specific heat capacity, β is the saline contraction coefficient, EP is the net freshwater exchange due to evaporation and precipitation (the ocean loses buoyancy with a positive $Q_{\text{net\_heat}}$ or a positive EP), and S is the sea surface salinity. $Q_{\text{net\_heat}}$ and EP are derived from the ERA5 data, and S is provided by the observations.

The dissipation rate by GI is calculated as (Large et al., 1994)

$$\epsilon_{GI} = \begin{cases} B_0 \dfrac{z+h}{h}, & -h \le z < 0 \text{ and } B_0 > 0 \\ 0 & z < -h \text{ or } B_0 < 0 \end{cases}. \tag{3}$$

The convective layer thickness, h, is determined by solving a quartic equation (Thomas et al., 2013),

$$\left(\frac{h}{H}\right)^4 - c^3\left(1 - \frac{h}{H}\right)^3 \left[\frac{w_*^3}{U^3} + \frac{u_*^2}{U^2}\cos\theta_w\right]^2 = 0, \tag{4}$$

when $B_0 > 0$ and EBF > 0, otherwise $h = H$. Here, $c = 14$ is an empirical constant, $w_* = (B_0 H)^{1/3}$ is the convective velocity due to surface buoyancy loss, θ_w is the angle between wind vectors and the vertical geostrophic shear direction, and $U = \frac{1}{f}\left|\int_{-H}^{0} b_r dz\right|$ is the velocity difference magnitude over the SI layer (b_r is the radial gradient of the buoyancy; Text S1 in Supporting Information S1).

2.1.3. Dissipation From Symmetric Instability

As one kind of submesoscale shear instability, symmetric instability (SI) feeds on the background vertical geostrophic shear at fronts with secondary circulation cells aligned along slanting isopycnals (Haine & Marshall, 1998; Stone, 1970). So, strong fronts accompanied by mesoscale eddies favor SI. Given that the growth of SI can be described by the geostrophic shear production, and assuming this production balances the SI dissipation rate, the dissipation rate can be parameterized as (Bachman et al., 2017; Thomas et al., 2013),

$$\epsilon_{SI} = \begin{cases} (EBF + B_0)\dfrac{z+H}{H} - B_0\dfrac{z+h}{h}, & -h \le z < 0 \\ (EBF + B_0)\dfrac{z+H}{H}, & -H \le z < -h \\ 0, & z < -H \end{cases}, \tag{5}$$

where EBF $= \boldsymbol{\tau}_w \times \mathbf{k}/(f\rho_0)\cdot\nabla_h b$ is the Ekman buoyancy flux related to Ekman transport across the tilt of isopycnals near the surface ($\nabla_h b$ is the horizontal buoyancy gradient, $b = -g\rho/\rho_0$ is the buoyancy). The along-front wind stress tends to weaken the stratification and strengthen the buoyancy gradient of fronts, favoring SI (Bachman et al., 2017). EBF can be calculated using the wind stress provided by the ERA5 and the buoyancy field from the observations. Note that Equation 5 is applied when B_0 and EBF are both positive (i.e., ocean heat loss and destabilization).

2.2. Data

2.2.1. In Situ Observations

In the winter of 2013–2014, two hydrographic sections were collected to investigate the surface dissipation across an anticyclonic eddy, which are an important component of the South China Sea Mesoscale Eddy Experiment (S-MEE) (Zhang et al., 2016). Profiles of temperature, salinity and turbulent dissipation in the upper 300 m along the two sections were collected by a MSS90 profiler (Sea & Sun Microstructure Profiler) and a CTD (Conductivity-Temperature-Depth Profiler). The profiles are averaged into 1-m bins in vertical. Velocity fields were sampled with a shipboard Teledyne RDI 75 kHz Acoustic Doppler Current Profiler (SADCP), transmitting in 16-m vertical bins with a sampling rate (i.e., ensemble interval; 12 pings for 12 s in each ensemble for average) of 1 min (the spatial resolution of the velocity is about 300 ∼ 500 m with an average ship speed of 4.5∼5 m s^{-1}). The sections were determined by near real-time sea level anomaly from the AVISO satellite altimeter data to direct the sections across the eddy center.

The first section (named S1, hereinafter) is a zonal section, which was conducted in 12/04–12/05, 2013 when the eddy was located in the west of the Luzon Strait (Figure 1a). S1 has nine stations with spatial intervals of approximately 21 ∼ 35 km (30 km on average). The second section (S2, hereinafter) was conducted meridionally in 1/14−1/16, 2014 when the eddy propagated to the west of the SCS basin (Figure 1f). S2 has 45 stations (27 MSS90 stations and 18 CTD stations) with spatial intervals of 5.5∼7.4 km (6.9 km on average). Horizontal velocities at the stations are obtained using the inverse distance weighting method (Shepard, 1968) with a search radius of 1 km.

2.2.2. ERA5 Reanalysis Data

To estimate contributions to the SML dissipation from different dynamical processes, hourly atmospheric and oceanic reanalysis data, namely, ERA5 of the European Centre for Medium-Range Weather Forecasts (ECMWF), were retrieved from the Copernicus Climate Change Service. ERA5 is the fifth generation reanalysis product provided by the ECMWF with a horizontal resolution of 0.25° × 0.25° for surface air-sea variables except 0.5° × 0.5° for wave parameters. ERA5 assimilates vast amounts of historical observations into global estimates (Hersbach et al., 2018). The atmospheric data include sea surface buoyancy fluxes (i.e., heat and freshwater fluxes), 10-m wind velocities, significant wave heights, peak wave periods and Stokes drift velocities. The wind stress is calculated as $\boldsymbol{\tau}_w = \rho_{\text{air}} C_d |\mathbf{u}_w| \mathbf{u}_w$, where ρ_{air} = 1.25 kg m^{-3}, C_{d} = 0.00125, and $\mathbf{u}_w$ are the air density, the drag coefficient, and the 10-m wind velocity, respectively. The atmospheric data along the sections are obtained by a linear interpolation according to the station locations and dates.

The corresponding surface quantities derived from the ERA5 data are shown in Figure S1 (Supporting Information S1). Due to the winter monsoon, the northeasterly wind over the SCS leads to negative wind stresses along the two sections (Figures S1a and S1d in Supporting Information S1). The significant wave height at S1 varies from 1.4 to 2 m, and from 2.2 to 4.4 m at S2 (Figures S1b and S1e in Supporting Information S1). The surface buoyancy flux B_0 is almost positive (i.e., buoyancy loss) at both sections, except for several stations with negative fluxes. By contrast, the Ekman buoyancy flux *EBF* is relatively weaker. One should note that the spatial variation of B_0 along the sections includes a time-aliasing effect (i.e., day-night cycle). The buoyancy fluxes are generally larger compared to Yang et al. (2017), which may be a result of the use of the hourly atmospheric ERA5 data compared to the 6-hours ERA Interim-Daily data set in Yang et al. (2017).

3. Results

The temperature, salinity, zonal and meridional velocities along the sections are shown in Figure 1. Corresponding to the positive sea surface anomaly, the SML deepens within the eddy (Figures 1b, 1c, 1g, and 1h). Over both sections, the SML thickness is generally shallower than 100 m at the eddy periphery but reaches more than 150 m at the center. The eddy circulation is seen in the northward current on the west of the eddy and southward toward the east along S1 with magnitudes up to 1.5 m s^{-1} near the surface (Figures 1d and 1e). The zonal current is weaker than the meridional current along S1, because this zonal section nearly bisects the eddy through its center. For the meridional section S2, zonal currents up to 1.5 m s^{-1} dominate with a westward flow on the north side but eastward on the south (Figures 1i and 1j). The meridional current is much weaker along section S2. The

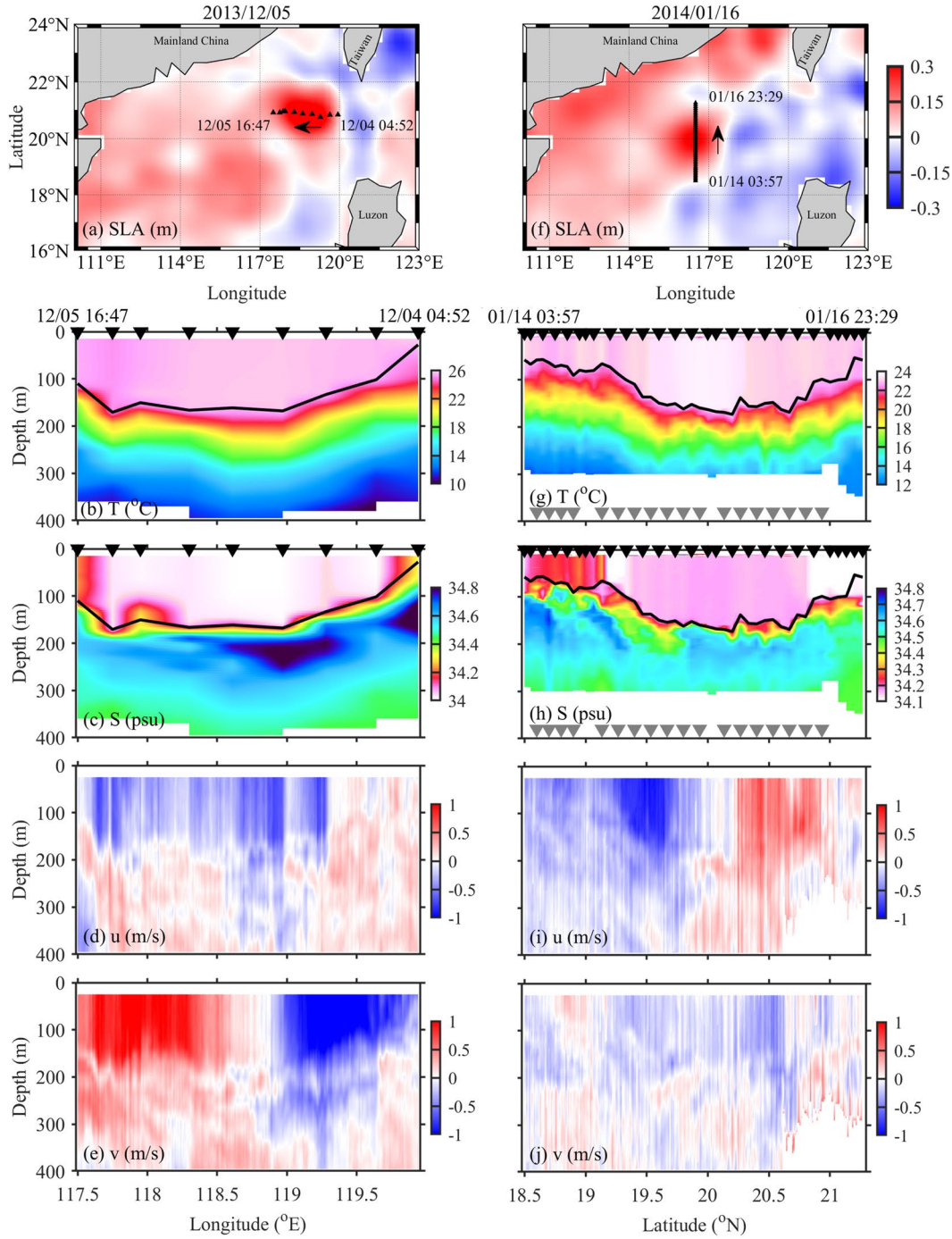

Figure 1. (a, f) Station locations (black triangles), (b, g) temperature (°C), (c, h) salinity (PSU), (d, i) zonal velocity (m s^{-1}; positive values indicate eastward direction), (e, j) meridional velocity (m s^{-1}; positive values indicate northward direction) along the sections (left: S1; right: S2). Color contours in (a, f) denote the sea level anomaly (m) from AVISO satellite altimeter data on 12/05/2013 and 01/16/2014, respectively. The arrows in (a, f) show the sections' direction with start and end dates shown. The MSS90 and CTD Profiler stations are denoted by black and gray triangles in (g, h). The black line in (b, c, g, h) denotes the surface mixed layer depth.

calculated buoyancy frequency N^2, gradient Richardson number Ri_g and the Rossby number Ro imply instabilities and submesoscales in the SML (i.e., $N^2 < 0$, $Ri_g < 1/4$, $|Ro| \sim 1$; Figure S2 in Supporting Information S1).

The Ertel potential vorticity (PV) is a key measure for instability analysis. Recently, Buckingham et al. (2021a, 2021b) proposed a criterion based on PV including the curvature effect for detecting instability types,

$$\Phi = (1 + \mathrm{Cu}) f q < 0. \tag{6}$$

Here, Cu is the flow curvature, f is the Coriolis parameter, q is the PV. Given that the sections cross the eddy center, Φ is evaluated in cylindrical coordinates and only the radial and vertical partial derivatives and the circulating velocity components are kept, namely, $\Phi=(1 + 2u^\theta/fr)[(f + u^\theta_r + u^\theta/r)b_z - u^\theta_z b_r]$ (Text S1 in Supporting Information S1). Here, u^θ_r and u^θ_z are the radial and vertical derivatives of the azimuthal velocity u^θ, b_r and b_z are the radial and vertical derivatives of the buoyancy b. An evaluation of the vertical vorticity by Zhong et al. (2017) indicated that this simplification is quantitatively close to the complete one at the eddy. Also following Zhong et al. (2017), u^θ/r is omitted within 5 km from the eddy center (the eddy center is defined as the zero-crossing point of the azimuthal velocity averaged in the upper 100 m along the sections). Despite that Cu is mostly negative (Figure S3 in Supporting Information S1), the factor, $L = 1 + \mathrm{Cu}$, is always greater than zero along the sections. The sign of Φ is totally determined by the sign of q compared to the sign of f. Hence, we directly analyze the sign of PV here. When $q < 0$, three possibilities occur: (a) it allows centrifugal/inertial instability (CI) if the negative value is from a large anticyclonic value of the vertical relative vorticity ζ ($\zeta = \partial u^\theta/\partial r + u^\theta/r$ in cylindrical coordinates), that is, $\zeta<-f$; (b) if $b_z < 0$, GI occurs; (c) a negative baroclinic term of the PV ($q_{bc} = -u^\theta_z b_r$) usually is associated with SI, that is, $q_{bc} < 0$.

As shown in Figures 2a and 2f, negative PV values are frequently observed in the SML. Based on these criteria, the instabilities can be classified (Figures 2b and 2g): (a) stable [or potentially geostrophic instability, mixed layer instability (MLI)]: $\Phi > 0$; (b) CI: $\zeta<-f$, $b_z > 0$, $q_{bc} > 0$; (c) GI: $\zeta > -f$, $b_z < 0$, $q_{bc} > 0$; (d) SI: $\zeta > -f$, $b_z > 0$, $q_{bc} < 0$; (e) SI&GI: $\zeta > -f$, $b_z < 0$, $q_{bc} < 0$; (f) SI&CI: $\zeta < -f$, $b_z > 0$, $q_{bc} < 0$. The conditions for instabilities can be observed at most stations of both sections, mainly concentrated in the SML. Below the SML, the negative PV is mainly a result of large negative ζ values or strong horizontal buoyancy gradients, indicating SI and CI. The percentages of the instability events are 48% (SI&CI), 27% (SI), 16% (SI&GI), 6% (GI), and 3% (CI) in the SML of S1 (64% of the SML observations are unstable; note that these numbers may be limited by the coarse resolution of S1, cf. 4.1.2). At S2, these percentages are 4% (SI&CI), 32% (SI), 45% (SI&GI), 18% (GI), and 1% (CI) (47% of the SML observations are unstable). Overall, the percentage of the instability events associated with SI exceeds 80% (91% at S1, 81% at S2), which is much higher than previous results in other observations, such as 40∼60% in the Atlantic Ocean (Buckingham et al., 2019) and the Pacific Ocean (Zhang et al., 2021). The higher percentage suggests that more active SI is favored within anticyclonic mesoscale eddies, and may be explained by outcropping isopycnals and strong submesoscale fronts observed along with anticyclonic mesoscale eddies (Figure 1; Brannigan et al., 2017; Zhong et al., 2017).

The observed dissipation rate along the sections is shown in Figures 2c and 2h. High dissipation rates are mainly confined in the SML and reach a magnitude of 10^{-5} W kg^{-1} near the surface, as much as four orders higher than those in the ocean interior. Elevated dissipation rates with magnitudes of 10^{-6} W kg^{-1} can be also observed within the ocean interior, such as the westernmost station of S1 and stations between 20.5 and 21°N at S2. At these regions, negative PV values associated with SI and CI are found. According to Figures 3d and 3e of Yang et al. (2017), sharp topography is observed just west of the westernmost station of the S1 section with a water depth about 690 m, while a seamount is located between 20.5 and 21°N in S2 with a water depth shallower than 300 m. So, the high dissipation found below the SML in these regions may be associated with current-topography interactions (Gula et al., 2015, 2016).

Within the SML but below 10 m, the vertically-integrated dissipation rates are in orders of 10^{-5}∼10^{-4} W m kg^{-1} (blue dots in Figures 2d and 2i). The estimated dissipation rates from the scalings in Section 2 combined with the forcing indicate that the SML process-based estimates are close to the observed dissipation rates (red dots show the estimates in Figures 2d and 2i). A comparison of the integral across the different contributions indicates that winds and waves are the dominant contributor of energy driving the SML dissipation (a comparison of the vertical profiles at certain stations between the observations and the scalings is also conducted, which is shown in Figure S4 in Supporting Information S1). The consistency between the observed and the calculated wind & wave-induced dissipation rates (Equation 1) suggests the parameterization scheme and forcing estimates capture

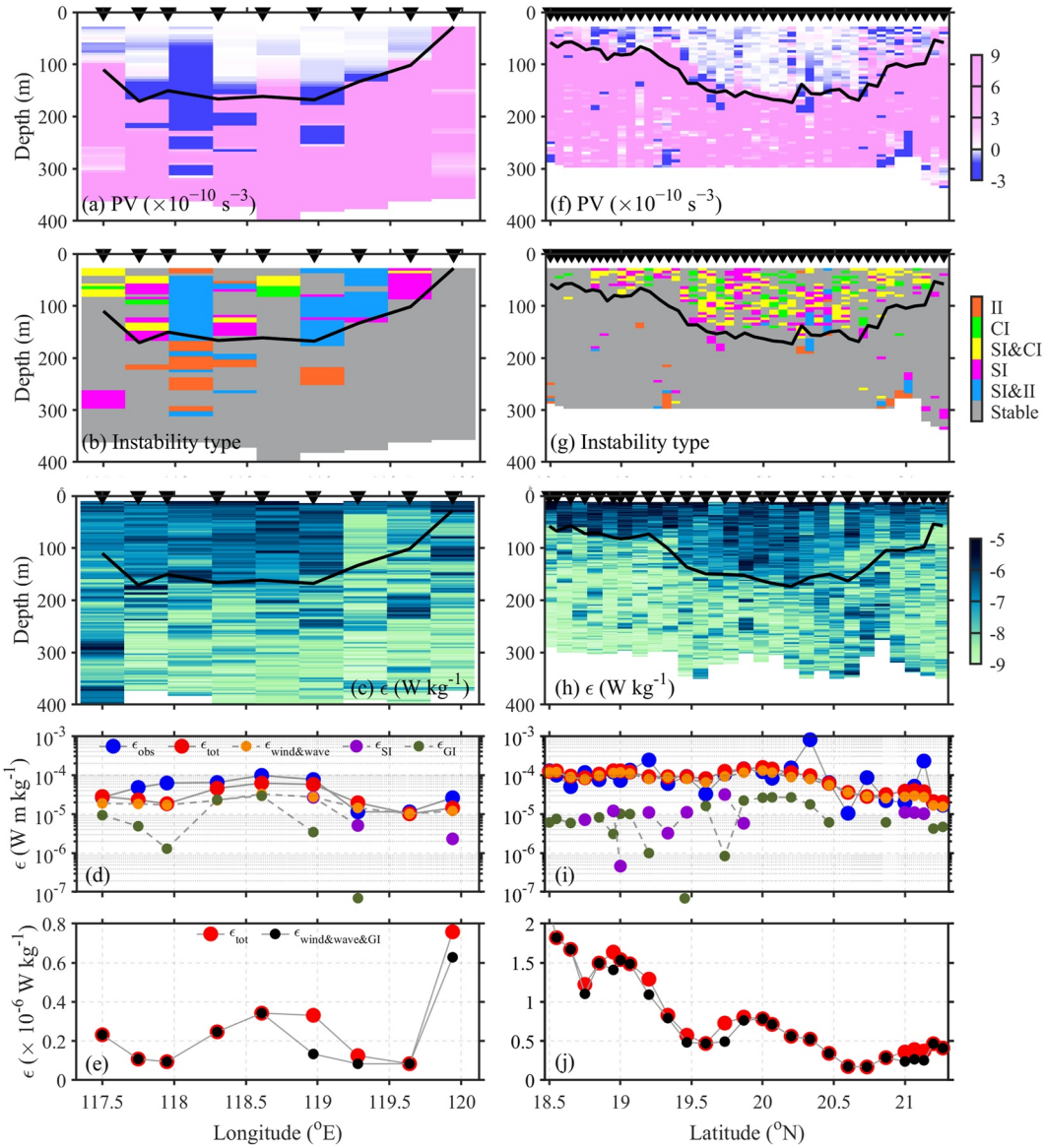

Figure 2. (a, c) Potential vorticity (×10^{-10} s^{-3}), (b, d) instability types, (c, h) observed dissipation rates ($log_{10}\varepsilon$; W kg^{-1}), (d, i) depth-integrated dissipation rates (W m kg^{-1}) within the surface mixed layer (SML), and (e, j) median values of the calculated dissipation rate (W kg^{-1}) within the SML along S1 (left panels) and S2 (right panels). The black line denotes the SML depth. The blue, red, yellow, pink and green dots in (d, i) denote integrals of the dissipation from the observations, all of the four SML processes, wind&wave, SI and GI, respectively. The green dots outside of penal (d, i) denotes the values of 5.5×10^{-10} W m kg^{-1} and 3.4×10^{-8} W m kg^{-1}, respectively. The red and black dots in (e, j) denote the medians of the total dissipation and the dissipation by the three SML processes not including SI deriving from the scaling methods. Only the parametrized dissipation rates at the MSS90 stations are shown at S2.

the basic level and variability of the dissipation from winds and waves, despite the use of the coarse resolution reanalysis data. SI and GI dissipations are not calculated at some stations where conditions on surface buoyancy fluxes aren't met. The calculated SI dissipation (Equation 5) has magnitudes of 10^{-6}~10^{-5} W m kg^{-1} and the calculated GI dissipation (Equation 3) is comparable with SI. The contributions from SI and GI to the SML dissipation are generally an order of magnitude below the observed values and the wind and wave estimates. A similar dominance of winds and waves in the SML dissipation and limited contributions from SI and GI have been reported by Buckingham et al. (2019) in the North Atlantic Ocean.

Despite the dominance of the wind and waves in the integrated SML dissipation, the effect of SI dissipation is highlighted by the median values of the SML dissipation that are calculated from the scaling methods (Figures 2e and 2j). Within section S1 the median dissipation rates at the stations with SI are elevated by 1.2 ∼ 2.5 times than those without SI (note again that the magnitude at S1 may be limited by the coarse resolution, cf. Section 4.1.2), while the largest dissipation enhancement due to SI also reaches 1.5 times higher at S2.

4. Discussion and Conclusions

4.1. Discussion

4.1.1. Effects of the Eddy

Using the same sections, Yang et al. (2017) reported elevated mixing at the eddy periphery by comparing dissipation profiles at the periphery and within the core. The enhancement is attributed to more active submesoscales at the periphery. As the SI activity has no preferred location across the eddy (Figures 2b and 2g), the active submesoscales at the periphery are very likely linked to MLI and frontogenesis. As shown in Figures 2d and 2i, the integral of the dissipation rate here shows no regular enhancement at the periphery: the integrated dissipation tends to be elevated at the eddy core compared to its periphery at S1 (the enhancement at the core may be partially explained by the deeper SML layer), but decreased from south to north at S2. So, the observed submesoscales at the periphery have limited contribution to the total dissipation within the SML, despite the fact that they elevate the local dissipation within the SML at the periphery. Up to now, no parameterization methods for scaling the dissipation from MLI and frontogenesis have been proposed. Despite that this contribution is likely rather limited given the good agreement between the observations and the wind&wave scaling, further study is needed to quantify the contribution from MLI and frontogenesis to the SML dissipation.

On the other hand, mesoscale eddies and currents do affect local surface winds and waves (e.g., Frenger et al., 2013; Ma et al., 2015; Marechal & de Marez, 2021; Wang et al., 2020), but these effects are not likely to be represented in the ERA5 wind and wave data used here. Despite the mesoscale-permitting resolution of the ERA data, our analysis indicates that no imprints from the mesoscale eddy are found in the wind and wave fields (Text S2 in Supporting Information S1). The consistency between the observed and parameterized dissipation rates suggests limited modulation by the mesoscale eddy on the SML dissipation by winds and waves.

Quantitatively, the analysis here shows that the mesoscale eddy modulates the SML dissipation by sometimes favoring SI, despite of the relatively small integrated dissipation magnitude compared with the observed wind&wave dissipation estimate. The horizontal buoyancy gradient across the eddy does provide negative PV and thus a favorable condition for SI occurrence.

Nevertheless, biases are still observed between the observed and parameterized dissipation. Noticeable biases exist at the stations in the west of S1. In addition to the accuracy limitation of the ERA data, one possible explanation is the incomplete parameterization of the SML processes. According to Figure 2, CI events accompanying strong negative PV are found at the west stations of S1, which is not included in the dissipation estimation. Another possibility is the interaction with topography, which is not estimated in this analysis.

4.1.2. SI Dissipation Magnitude

The magnitude of SI dissipation from the scaling tightly depends on the lateral buoyancy gradient. Submesoscale fronts are captured at S2 due to its fine resolution (Zhong et al., 2017). The submesoscale buoyancy variance is mainly attributed to MLI and frontogenesis, which usually have relatively larger spatial scales (Dong et al., 2020), since the SI spatial scale is generally below 10 km (Text S3 in Supporting Information S1) and cannot be resolved by the observations. However, the estimation of SI dissipation is potentially limited by the coarse resolution of S1 which can only capture the mesoscale buoyancy variance across the eddy (Figure S6 in Supporting Information S1).

So, the following discussion is only based on the result at S2. The SML depth-integrated dissipation rate of SI averaged over all stations of S2 is 4.3×10^{-6} W m kg^{-1} with a maximum of 3.2×10^{-5} W m kg^{-1}. This magnitude is relatively large compared to most previous studies. A larger dissipation rate of approximately 2.5×10^{-4} W m kg^{-1} due to SI was observed at a strong front in the Kuroshio region by D'Asaro et al. (2011). In the Southern Ocean, Yu et al. (2019) reported a maximum observed dissipation rate of approximately 5.5×10^{-5} W m kg^{-1} during SI

events, which is in the same order as the magnitude here. The SI dissipation has been also estimated using the scaling method (Equation 5) on the basis of high-resolution models (i.e., Buckingham et al., 2019; Dong et al., 2021). Buckingham et al. (2019) estimated an annual magnitude of SI dissipation up to 4.2×10^{-7} W m kg^{-1} in the north Atlantic Ocean. According to Dong et al. (2021), a global estimate of the SI dissipation is 8.3×10^{-7} W m kg^{-1}. So, the SI dissipation rate at the eddy is one order of magnitude larger compared to the long-term or global-scale estimates. It is expected that the SI dissipation would be highly intermittent (Pearson & Fox-Kemper, 2018), and thus the large-scale average would be supported by only a few sites, potentially the values within eddies such as this one being part of the greater-than-average contributions. Moreover, the magnitude of the SI dissipation is derived based on observational sections in winter. The SI dissipation is expected to become weaker in summer due to the SML shoaling (Buckingham et al., 2019; Dong et al., 2021).

Considering that EBF is much smaller compared with B_0 (Figure S1 in the Supporting Information S1), it is reasonable to assume that the energy extracted by SI that leads to the SI dissipation is mainly from the background geostrophic shear at the eddy (including the contribution from the eddy but also the submesoscales). The kinetic energy density at the eddy in the SML of S2 is 0.11 J kg^{-1}. The mean SI dissipation rate is 3.6×10^{-8} W kg^{-1} as the averaged SML depth is 118 m. As a result, it would take about 35 days for SI dissipation at this intensity to dissipate all of the kinetic energy at the eddy in the SML. This rough estimate overlooks many of the complex processes and variations in forcing during the eddy propagation. Nevertheless, the SI does play a role in the eddy energy budget.

5. Conclusions

Based on two observational sections across an anticyclonic eddy in the SCS including observed dissipation rates, contributions from different SML processes to the SML dissipation are estimated, and the potential modulation by the eddy on the SML dissipation is discussed.

Negative PV values are frequently observed in the SML along the two sections according to the calculated PV. An investigation of the negative PV values indicates different types of instabilities, including SI, CI, and GI. The SI events account for more than 80% at times with negative PV values at the sections. Based on the scaling method, the dissipation rate integrated in the SML is in orders of $10^{-5} \sim 10^{-4}$ W m kg^{-1}, which closely matches the estimated contributions from winds and waves. Dissipation from SI and GI indicates they contribute less toward dissipation than winds and waves. Only limited modulation of the eddy on the winds and waves, and thus dissipation from winds and waves, is permitted by the close match of observed and estimated wind and wave dissipation.

The work highlights active SI events at the eddy with an averaged depth-integrated dissipation rate of 4.3×10^{-6} W m kg^{-1} and a maximum of 3.2×10^{-5} W m kg^{-1} in the SML over all stations of S2. It is found that the median dissipation rates at stations with SI are elevated by up to 1.5 times at S2. The dissipation rate from SI is believed to potentially modulate the eddy kinetic energy budget and dissipation.

In this work, SI is demonstrated to be active at mesoscale eddies, at least anticyclonic eddies, and the SI contribution to the SML dissipation is investigated. Meanwhile, SI also enhances vertical and cross-front material transports (e.g., Dong et al., 2021; Wenegrat et al., 2020). It is still unclear the role of these effects on materials trapped within an eddy, and more comprehensive future observations are needed to address that problem.

Data Availability Statement

The data for reproducing the results of this work is available at https://doi.org/10.5281/zenodo.6919450. The ERA5 can be retrieved at https://cds.climate.copernicus.eu/cdsapp#!/dataset/reanalysis-era5-single-levels?tab=-form. The sea level anomaly from AVISO satellite altimeter data is available at https://resources.marine.copernicus.eu/product-detail/SEALEVEL_GLO_PHY_L4_MY_008_047/DATA-ACCESS.

Acknowledgments
The authors thank two anonymous reviewers for their valuable comments and thoughtful suggestions. This work is supported by the National Natural Science Foundation of China (91958205; 42176023; 92058201), the National Key Research and Development Program of China (2017YFA0604100) and the State Key Laboratory of Tropical Oceanography, South China Sea Institute of Oceanology, Chinese Academy of Sciences (LTO2101). BFK is supported by NOAA NA19OAR4310366.

References

Bachman, S. D., Fox-Kemper, B., Taylor, J. R., & Thomas, L. N. (2017). Parameterization of frontal symmetric instabilities. I: Theory for resolved fronts. *Ocean Modelling*, *109*, 72–95. https://doi.org/10.1016/j.ocemod.2016.12.003

Brannigan, L., Marshall, D. P., Naveira Garabato, A. C., Nurser, A. J. G., & Kaiser, J. (2017). Submesoscale instabilities in mesoscale eddies. *Journal of Physical Oceanography*, *47*(12), 3061–3085. https://doi.org/10.1175/JPO-D-16-0178.1

Buckingham, C. E., Gula, J., & Carton, X. (2021a). The role of curvature in modifying frontal instabilities. Part I: Review of theory and presentation of a nondimensional instability criterion. *Journal of Physical Oceanography*, *51*(2), 299–315. https://doi.org/10.1175/JPO-D-19-0265.1

Buckingham, C. E., Gula, J., & Carton, X. (2021b). The role of curvature in modifying frontal instabilities. Part II: Application of the criterion to curved density fronts at low Richardson numbers. *Journal of Physical Oceanography*, *51*(2), 317–341. https://doi.org/10.1175/JPO-D-20-0258.1

Buckingham, C. E., Lucas, N., Belcher, S., Rippeth, T., Grant, A., Le Sommer, J., et al. (2019). The contribution of surface and submesoscale processes to turbulence in the open ocean surface boundary layer. *Journal of Advances in Modeling Earth Systems*, *11*(12), 4066–4094. https://doi.org/10.1029/2019MS001801

Chen, G., Hou, Y., & Chu, X. (2011). Mesoscale eddies in the South China Sea: Mean properties, spatiotemporal variability, and impact on thermohaline structure. *Journal of Geophysical Research*, *116*(C6), C06018. https://doi.org/10.1029/2010JC006716

D'Asaro, E., Lee, C., Rainville, L., Harcourt, R., & Thomas, L. (2011). Enhanced turbulence and energy dissipation at ocean fronts. *Science*, *332*(6027), 318–322. https://doi.org/10.1126/science.1201515

de Boyer Montégut, C., Madec, G., Fischer, A. S., Lazar, A., & Iudicone, D. (2004). Mixed layer depth over the global ocean: An examination of profile data and a profile-based climatology. *Journal of Geophysical Research*, *109*(C12), C12003. https://doi.org/10.1029/2004JC002378

Dong, C., McWilliams, J. C., Liu, Y., & Chen, D. (2014). Global heat and salt transports by eddy movement. *Nature Communications*, *5*(1), 1–6. https://doi.org/10.1038/ncomms4294

Dong, J., Fox-Kemper, B., Zhang, H., & Dong, C. (2020). The scale of submesoscale baroclinic instability globally. *Journal of Physical Oceanography*, *50*(9), 2649–2667. https://doi.org/10.1175/JPO-D-20-0043.1

Dong, J., Fox-Kemper, B., Zhang, H., & Dong, C. (2021). The scale and activity of symmetric instability estimated from a global submesoscale-permitting ocean model. *Journal of Physical Oceanography*, *51*(5), 1655–1670. https://doi.org/10.1175/JPO-D-20-0159.1

Dong, J., Fox-Kemper, B., Zhu, J., & Dong, C. (2021). Application of symmetric instability parameterization in the Coastal and Regional Ocean Community Model (CROCO). *Journal of Advances in Modeling Earth Systems*, *13*(3). Portico. https://doi.org/10.1029/2020ms002302

Fox-Kemper, B., Danabasoglu, G., Ferrari, R., Griffies, S. M., Hallberg, R. W., Holland, M. M., et al. (2011). Parameterization of mixed layer eddies. III: Implementation and impact in global ocean climate simulations. *Ocean Modelling*, *39*(1–2), 61–78. https://doi.org/10.1016/j.ocemod.2010.09.002

Fox-Kemper, B., Ferrari, R., & Hallberg, R. (2008). Parameterization of mixed layer eddies. Part I: Theory and diagnosis. *Journal of Physical Oceanography*, *38*(6), 1145–1165. https://doi.org/10.1175/2007JPO3792.1

Frenger, I., Gruber, N., Knutti, R., & Münnich, M. (2013). Imprint of Southern Ocean eddies on winds, clouds and rainfall. *Nature Geoscience*, *6*(8), 608–612. https://doi.org/10.1038/ngeo1863

Gaube, P., McGillicuddy, D. J., Jr., & Moulin, A. J. (2019). Mesoscale eddies modulate mixed layer depth globally. *Geophysical Research Letters*, *46*(3), 1505–1512. https://doi.org/10.1029/2018GL080006

Grant, A. L. M., & Belcher, S. E. (2009). Characteristics of Langmuir turbulence in the ocean mixed layer. *Journal of Physical Oceanography*, *39*(8), 1871–1887. https://doi.org/10.1175/2009jpo4119.1

Gula, J., Molemaker, M., & McWilliams, J. (2015). Topographic vorticity generation, submesoscale instability and vortex street formation in the Gulf Stream. *Geophysical Research Letters*, *42*(10), 4054–4062. https://doi.org/10.1002/2015GL063731

Gula, J., Molemaker, M. J., & McWilliams, J. C. (2016). Topographic generation of submesoscale centrifugal instability and energy dissipation. *Nature Communications*, *7*(1), 12811. https://doi.org/10.1038/ncomms12811

Haine, T. W. N., & Marshall, J. (1998). Gravitational, symmetric, and baroclinic instability of the ocean mixed layer. *Journal of Physical Oceanography*, *28*(4), 634–658. https://doi.org/10.1175/1520-0485(1998)028<0634:GSABIO>2.0.CO;2

Haney, S., Fox-Kemper, B., Julien, K., & Webb, A. (2015). Symmetric and geostrophic instabilities in the wave-forced ocean mixed layer. *Journal of Physical Oceanography*, *45*(12), 3033–3056. https://doi.org/10.1175/JPO-D-15-0044.1

Hara, T., & Belcher, S. E. (2004). Wind profile and drag coefficient over mature ocean surface wave spectra. *Journal of Physical Oceanography*, *34*(11), 2345–2358. https://doi.org/10.1175/JPO2633.1

Hersbach, H., Bell, B., Berrisford, P., Biavati, G., Horányi, A., Muñoz Sabater, J., et al. (2018). ERA5 hourly data on single levels from 1979 to present. *Copernicus Climate Change Service (C3S) Climate Data Store (CDS)*. https://doi.org/10.24381/cds.adbb2d47

Large, W. G., McWilliams, J. C., & Doney, S. C. (1994). Oceanic vertical mixing: A review and a model with a nonlocal boundary layer parameterization. *Reviews of Geophysics*, *32*(4), 363–403. https://doi.org/10.1029/94RG01872

Legg, S., McWilliams, J., & Gao, J. (1998). Localization of deep ocean convection by a mesoscale eddy. *Journal of Physical Oceanography*, *28*(5), 944–970. https://doi.org/10.1175/1520-0485(1998)028<0944:Lodocb>2.0.Co;2

Li, Q., Webb, A., Fox-Kemper, B., Craig, A., Danabasoglu, G., Large, W. G., & Vertenstein, M. (2016). Langmuir mixing effects on global climate: WAVEWATCH III in CESM. *Ocean Modelling*, *103*, 145–160. https://doi.org/10.1016/j.ocemod.2015.07.020

Lin, X., Dong, C., Chen, D., Liu, Y., Yang, J., Zou, B., & Guan, Y. (2015). Three-dimensional properties of mesoscale eddies in the South China Sea based on eddy-resolving model output. *Deep Sea Research Part I: Oceanographic Research Papers*, *99*, 46–64. https://doi.org/10.1016/j.dsr.2015.01.007

Ma, J., Xu, H., Dong, C., Lin, P., & Liu, Y. (2015). Atmospheric responses to oceanic eddies in the Kuroshio Extension region. *Journal of Geophysical Research: Atomsphere*, *120*(13), 6313–6330. https://doi.org/10.1002/2014JD022930

Marechal, G., & de Marez, C. (2021). Variability of wind wave field by realistic mesoscale and submesoscale eddy field. *Ocean Science Discussions*, 1–18. https://doi.org/10.5194/os-2021-53

McWilliams, J. C. (2016). Submesoscale currents in the ocean. *Proceedings of the Royal Society A: Mathematical, Physical and Engineering Sciences*, *472*(2189), 20160117. https://doi.org/10.1098/rspa.2016.0117

Melville, W. K. (1996). The role of surface-wave breaking in air-sea interaction. *Annual Review of Fluid Mechanics*, *28*(1), 279–321. https://doi.org/10.1146/annurev.fl.28.010196.001431

Noh, Y., Ok, H., Lee, E., Toyoda, T., & Hirose, N. (2016). Parameterization of Langmuir circulation in the ocean mixed layer model using LES and its application to the OGCM. *Journal of Physical Oceanography*, *46*(1), 57–78. https://doi.org/10.1175/JPO-D-14-0137.1

Pearson, B., & Fox-Kemper, B. (2018). Log-normal turbulence dissipation in global ocean models. *Physical Review Letters*, *120*(9), 094501. https://doi.org/10.1103/PhysRevLett.120.094501

Qiao, F., Yuan, Y., Deng, J., Dai, D., & Song, Z. (2016). Wave–turbulence interaction-induced vertical mixing and its effects in ocean and climate models. *Philosophical Transactions of the Royal Society A: Mathematical, Physical and Engineering Sciences*, *374*(2065), 20150201. https://doi.org/10.1098/rsta.2015.0201

Shepard, D. (1968). A two-dimensional interpolation function for irregularly-spaced data. *Proceedings of the 1968 23rd ACM national conference*, 517–524. https://doi.org/10.1145/800186.810616

Stone, P. H. (1970). On non-geostrophic baroclinic stability: Part II. *Journal of the Atmospheric Sciences*, *27*(5), 721–726. https://doi.org/10.1175/1520-0469(1970)027<0721:ONGBSP>2.0.CO;2

Terray, E. A., Donelan, M. A., Agrawal, Y. C., Drennan, W. M., Kahma, K. K., Williams, A. J., et al. (1996). Estimates of kinetic energy dissipation under breaking waves. *Journal of Physical Oceanography*, *26*(5), 792–807. https://doi.org/10.1175/1520-0485(1996)026<0792:Eokedu>2.0.Co;2

Thomas, L. N., Taylor, J. R., Ferrari, R., & Joyce, T. M. (2013). Symmetric instability in the Gulf Stream. *Deep Sea Research Part II: Topical Studies in Oceanography*, *91*, 96–110. https://doi.org/10.1016/j.dsr2.2013.02.025

Thorpe, S. (2004). Langmuir circulation. *Annual Review of Fluid Mechanics*, *36*(1), 55–79. https://doi.org/10.1146/annurev.fluid.36.052203.071431

Wang, J., Dong, C., & Yu, K. (2020). The influences of the Kuroshio on wave characteristics and wave energy distribution in the East China Sea. *Deep-Sea Research Part I Oceanographic Research Papers*, *158*, 103228. https://doi.org/10.1016/j.dsr.2020.103228

Wenegrat, J. O., Thomas, L. N., Sundermeyer, M. A., Taylor, J. R., D'Asaro, E. A., Klymak, J. M., et al. (2020). Enhanced mixing across the gyre boundary at the Gulf Stream front. *Proceedings of the National Academy of Sciences of the United States of America*, *117*(30), 17607–17614. https://doi.org/10.1073/pnas.2005558117

Yang, Q., Nikurashin, M., Sasaki, H., Sun, H., & Tian, J. (2019). Dissipation of mesoscale eddies and its contribution to mixing in the northern South China Sea. *Scientific Reports*, *9*(1), 1–9. https://doi.org/10.1038/s41598-018-36610-x

Yang, Q., Zhao, W., Liang, X., Dong, J., & Tian, J. (2017). Elevated mixing in the periphery of mesoscale eddies in the South China Sea. *Journal of Physical Oceanography*, *47*(4), 895–907. https://doi.org/10.1038/s41598-018-36610-x

Yu, X., Naveira Garabato, A. C., Martin, A. P., Gwyn Evans, D., & Su, Z. (2019). Wind-forced symmetric instability at a transient mid-ocean front. *Geophysical Research Letters*, *46*(20), 11281–11291. https://doi.org/10.1029/2019GL084309

Zhang, Z., Tian, J., Qiu, B., Zhao, W., Chang, P., Wu, D., & Wan, X. (2016). Observed 3D structure, generation, and dissipation of oceanic mesoscale eddies in the South China Sea. *Scientific Reports*, *6*(1), 24349. https://doi.org/10.1038/srep24349

Zhang, Z., Wang, W., & Qiu, B. (2014). Oceanic mass transport by mesoscale eddies. *Science*, *345*(6194), 322–324. https://doi.org/10.1126/science.1252418

Zhang, Z., Zhang, X., Qiu, B., Zhao, W., Zhou, C., Huang, X., & Tian, J. (2021). Submesoscale currents in the subtropical upper ocean observed by long-term high-resolution mooring arrays. *Journal of Physical Oceanography*, *51*, 1–65. https://doi.org/10.1175/jpo-d-20-0100.1

Zhong, Y., Bracco, A., Tian, J., Dong, J., Zhao, W., & Zhang, Z. (2017). Observed and simulated submesoscale vertical pump of an anticyclonic eddy in the South China Sea. *Scientific Reports*, *7*(1), 44011. https://doi.org/10.1038/srep44011